Research Square

Preprints are preliminary reports that have not undergone peer review.
They should not be considered conclusive, used to inform clinical practice,
or referenced by the media as validated information.

Structural basis of IgLON5 autoantibody recognition in autoimmune encephalitis

Laurent Perez

laurent.perez@chuv.ch

Lausanne University Hospital and University of Lausanne, https://orcid.org/0000-0002-8860-7928

Angelique Roux Roux

Lausanne University Hospital and University of Lausanne,

Rachel Schelling

CHUV https://orcid.org/0000-0001-6966-6626

David Vinyals-Sales

Lausanne University Hospital and University of Lausanne,

Lidia Sabater

Hospital Clínic de Barcelona

Rahel Winiger

Lausanne University Hospital and University of Lausanne,

Ilayda Senyuz

Lausanne University Hospital and University of Lausanne,

Alison Lin

Lausanne University Hospital and University of Lausanne,

Amandine MATHIAS

Laboratory of Neuroimmunology, Neuroscience Research Centre, Department of Clinical Neurosciences, University Hospital and University of Lausanne https://orcid.org/0009-0005-3604-5096

Renaud DU PASQUIER

Laboratory of Neuroimmunology, Neuroscience Research Centre, Department of Clinical Neurosciences, University Hospital and University of Lausanne https://orcid.org/0000-0002-2786-3434

CARLES GAIG

Hospital Clinic of Barcelona

Josep Dalmau

ICREA-Institut d'Investigacions Biomèdiques August Pi i Sunyer https://orcid.org/0000-0001-5856-2813

Mathilde Foglierini

CHUV https://orcid.org/0000-0001-7538-4262

Article

Keywords: IgLON5, Neurodegeneration, CryoEM, Immune repertoire, antigen-antibody complex

Posted Date: April 27th, 2026

DOI: https://doi.org/10.21203/rs.3.rs-9427214/v1

License: This work is licensed under a Creative Commons Attribution 4.0 International License.
Read Full License

Additional Declarations: There is **NO** Competing Interest.

Abstract

Anti-IgLON5 disease is a rare neurological disorder at the interface of autoimmunity and neurodegeneration. It is characterized by autoantibodies against the neuronal adhesion molecule IgLON5 and is associated with profound brain dysfunction and tau pathology. Despite its severe clinical manifestations, the molecular basis of antibody recognition and its contribution to disease pathogenesis remain unclear. Here, we profile the B cell receptor repertoire of a patient with anti-IgLON5 disease and identify a highly polyclonal response lacking dominant clonal expansion. We isolate a human monoclonal IgG4 antibody that binds IgLON5 with high affinity and determine its structure in complex with IgLON5 by cryo–electron microscopy. Biochemical and structural analyses show that antibody binding preserves IgLON5 adhesion interfaces while promoting higher-order clustering of IgLON5 dimers. These findings provide mechanistic insight into autoantibody recognition of neuronal surface proteins and establish a framework for understanding antibody-mediated neurodegeneration in anti-IgLON5 disease.

Introduction

IgLON proteins comprise a family of immunoglobulin-like cell adhesion molecules (CAMs) predominantly localized to neuronal membranes, where they contribute to the organization and maintenance of nervous system architecture[1,2]. They play key roles in regulating neuronal arborization, supporting the formation and maintenance of excitatory synapses, and modulating neuronal connectivity and network stability[3-7]. The protein family comprises five members: opioid-binding protein/cell adhesion molecule-like (OPCML/IgLON1), neurotrimin (NTM/IgLON2), limbic system-associated membrane protein (LSAMP/IgLON3), neuronal growth regulator 1 (NEGR1/IgLON4), and IgLON5[8]. They all share a high degree of structural similarity with a length of about 340 amino acids divided in three extracellular immunoglobulin (Ig)-like domains of the C2 type followed by a short stalk and a glycosylphosphatidylinositol (GPI)-anchor[9,10]. All IgLON family members assemble into homo- and heteromeric complexes, engaging in both *cis* and *trans* interactions to mediate cell–cell adhesion and regulate neuronal connectivity[11,12]. IgLON dimerization is mediated by the first Ig domains, with the two protomers associating in a “head-to-head” configuration[13]. These *trans* interactions (across opposing membranes) generate a V-shaped complex compatible with synaptic cleft dimensions and likely contribute to the organization of chemical synapses[14].

Among the IgLON family members, IgLON5 has attracted particular attention following the identification of anti-IgLON5 disease, a rare but severe neurological disorder characterized by the presence of IgG autoantibodies targeting IgLON5 in both cerebrospinal fluid and serum[15]. Clinically, patients present with a heterogeneous constellation of symptoms, including rapid eye movement (REM) and non-REM parasomnias, sleep-apneas, bulbar dysfunction, gait instability, and abnormal movements, mainly facial dyskinesias and chorea[16,17]. The disorder frequently evolves into a neurodegenerative state marked by neuronal accumulation of hyperphosphorylated tau across multiple regions of the central nervous

system with preference in the tegmentum of the brainstem, hypothalamus, and spinal cord[18,19]. Notably, the disease exhibits a strong genetic association with specific human leukocyte antigen (HLA) haplotypes, particularly HLA-DRB1*10:01 and DQB1*05:01, supporting a role for genetic predisposition in disease susceptibility and highlighting a link between autoimmune mechanisms and neurodegeneration[20]. Similarly to other autoimmune encephalitis syndromes, such as LGI1 (leucine-rich glioma-inactivated 1) and CASPR2 (contactin-associated protein-like 2) diseases, autoantibodies predominantly belong to the IgG4 subclass, although IgG1 antibodies have also been reported[21,22]. IgG4 responses are typically associated with chronic antigen exposure and are characterized by limited effector functions, including a reduced capacity to activate complement and engage Fc receptors[23], suggesting that disease mechanisms may extend beyond classical antibody-mediated cytotoxicity. Despite the severity and progressive nature of the disorder, the fundamental immunological and molecular pathways driving disease pathogenesis remain poorly defined, and current therapeutic approaches have demonstrated only modest efficacy[24,25].

Recent studies have demonstrated that polyclonal IgG isolated from patient sera can disrupt trans-synaptic interactions and induce a sustained reduction of IgLON5 clusters at the neuronal surface, thereby underscoring the critical role of IgLON5 in maintaining neuronal connectivity[26,27]. Furthermore, exposure of neurons to anti-IgLON5 antibodies results in neurodegenerative alterations, including membrane blebbing and neuritic fragmentation probably leading to increased tau hyperphosphorylation and ultimately neuronal cell death, as shown in autopsy studies[28,29]. These effects are thought to arise from antibody-induced neuronal hyperactivity, which promotes somatodendritic tau missorting and aggregation[30]. Interestingly, distinct mechanisms of action have been proposed depending on the immunoglobulin subclass involved: IgG1 antibodies have been shown to induce irreversible internalization of IgLON5 clusters, whereas IgG4 antibodies are more likely to interfere with protein–protein interactions[31]. Clinically and neuropathologically, the disease represents a unique form of tauopathy that differs from classical primary tauopathies such as Alzheimer's disease, progressive supranuclear palsy (PSP), and corticobasal degeneration (CBD). IgLON5 tauopathy is characterized by the accumulation of both 3R and 4R tau isoforms, yet displays a distinct anatomical distribution, differing from the cortical predominance observed in Alzheimer's disease and the basal ganglia–frontal involvement typical of PSP and CBD[19,29,32]. Collectively, these findings support a model in which tau deposition in IgLON5 disease arises secondary to chronic antibody-mediated synaptic dysfunction, rather than reflecting a primary tau-driven neurodegenerative process.

Most studies investigating IgLON5 autoimmunity and antibody binding have relied on polyclonal IgG purified from patient sera. While informative, such approaches preclude the precise dissection of individual antibody specificities and limit detailed structural and mechanistic characterization of IgLON5 recognition. In this study, we dissected the B cell repertoire of a patient with anti-IgLON5 disease, revealing a diverse, polyclonal IgG4-skewed response. Despite the lack of dominant clonal expansion, we isolated a high-affinity monoclonal antibody, suggesting that pathogenic activity may be driven by individual clones embedded within a broadly heterogeneous repertoire. Using single-particle cryo–

electron microscopy (cryo-EM), we resolved the structure of the IgLON5–Fab complex at 3.7 Å resolution, revealing that the antibody targets a broad conformational epitope within the second Ig-like domain. Importantly, our data demonstrate that Fab binding does not interfere with IgLON5 homo- or heterodimerization, indicating that pathogenicity is unlikely to arise from direct disruption of adhesion interfaces. Instead, structural organization combined with *in vitro* assays supports a model in which bivalent antibody binding promotes higher-order clustering of IgLON5 homo- and heterodimers, thereby providing a structural basis for antibody-driven synaptic reorganization.

Results

Characterization of the B cell receptor repertoire in anti-IgLON5 disease

To identify anti-IgLON5 monoclonal antibodies (mAbs), we sequenced the B cell receptor (BCR) repertoire from a 60-year-old male patient diagnosed with anti IgLON5 disease. Memory B cells isolated from peripheral blood mononuclear cells (PBMCs) of donor D1 were FACS sorted and subjected to single-cell BCR sequencing using the 10x Genomics platform. After filtering productive paired heavy and light chains sequences, we successfully reconstructed a set of 9577 immunoglobulin sequences from the donor, including 968 antigens specific (**Supplementary Fig. 1**). As a negative control, we used previously reported BCR repertoires from two healthy donors, matched for cell counts (H1 and H2)[33]. To assess BCR repertoire diversity across donors, we used coverage-based rarefaction analysis with Hill numbers. The estimated sample coverage ranged from ~0.10 to ~0.45 (**Supplementary Fig. 2a**) and despite incomplete sampling, D1 consistently exhibited the highest clonal diversity based on clonal richness (Hill q = 0) and Shannon diversity (Hill q = 1), compared to H1 and H2 (**Supplementary Fig. 2b-c**). This result, suggest a broader and more evenly distributed BCR repertoire in D1 and an absence of strong clonal expansion. The variable heavy (VH) gene usage was broadly similar across donors (**Figure. 1a**), except for a notable overrepresentation of VH1-69 in D1 relative to healthy controls. The light variable (VL) V gene usage was equally comparable, with no major differences in Kappa or Lambda gene frequencies across the three donors (**Supplementary Fig. 3**). Beyond V gene usage, isotype distribution was also largely conserved, with IgM^+ clonotypes predominating across all donors and reaching 47.3% of the donor D1 repertoire. The IgA1 and IgA2 subtypes frequencies were modestly elevated in D1 (22% and 14.8%, respectively) relative to healthy donors (**Figure. 1b**). Surprisingly, only a slight increase in the IgG4 subtype was observed in the IgLON5 patient repertoire (D1: 0.9%; H1: 0.6%; H2: 0.7%). Consistent with the overall similarity in repertoire features, the length distribution of the third complementarity-determining region of the heavy chain (CDRH3) followed a normal distribution, with a median length of 15 residues across all donors (**Figure. 1c**). To assess the somatic mutation frequency, we first excluded clonotypes with a mutation frequency of zero, which likely included naive B cells, highly abundant in the donor D1 (25%) compared to healthy donors (H1: 3.4% and H2: 5.6%). Interestingly, the mutation frequency differed significantly across donors ($p < 0.0001$) and Post hoc Games–Howell testing showed that D1 had a significantly higher mean mutation frequency than both healthy donors (vs H1 and H2, $p < 0.0001$), whereas no significant difference was observed between them (H1 vs H2: $p = 0.087$). The mean

mutation frequency in D1 was 0.121 ± 0.061, compared to 0.096 ± 0.050 in H1 and 0.098 ± 0.053 in H2 (**Figure. 1d**). Of note, this higher mutation frequency in D1 is consistent with previously reported increased frequency of somatic hypermutation in the context of autoimmune diseases due to chronic antigenic stimulation[34]. To define clonal relationships, we applied the Immcantation suite to reconstruct clonal families and represent the CDRH3 sequences as a clonal network (**Figure. 1e**). A total of 7,858 clonal families were identified, illustrating a highly polyclonal BCR repertoire (**Figure. 1f**). The large clonal families (>5 cells) accounted for only 7.5% of total memory B cells and were predominantly of IgM isotype (68.6%). A smaller proportion of IgA clones (29.4%) and only rare IgG families were also detected. One prominent exception was a large clonal family of 80 IgM clonotypes utilizing VH1-69, consistent with the global overrepresentation of this gene segment in D1. As the disease is characterized by a predominance of IgG4 antibodies, we focused on this subclass and identified 86 paired sequences, including five antigen-specific sequences. The majority of IgG4 clones were singletons (one clonal family of size 3 and two of size 2) and heavy chain V–J gene combinations were highly heterogeneous (**Figure. 1g**). We then verified the specificity of the five antigen-specific clones by ELISA and confirmed the reactivity of one clone. Interestingly, the specific clone (mAb2513) utilized a VH derived from the germline gene IGHV4-39, which has been previously reported in several autoimmune conditions, including multiple sclerosis, where it has been associated with autoreactive B-cell responses[35]. The inference of the unmutated common ancestor (UCA) for this clone (VH4-39/JH4 and VK3-20/JK3) revealed a somatic mutation frequency of 0.12, consistent with good affinity maturation of the clone (**Figure. 1h**).

Biochemical characterisation of mAb2513 and IgLON5 interaction

To validate the reactivity of the VH4-39 BCR, we first generated a construct encoding the extracellular domain of human IgLON5 truncated at the ω-site (residue 316) to prevent glycosylphosphatidylinositol anchoring. We also added a Fc domain at the C-terminus, to ease protein secretion and purification. The protein was produced by transient transfection of Expi293 cells, purified by Protein A resin, and subsequently papain cleaved to remove the Fc tag. We next evaluated complex formation in solution using size-exclusion chromatography (SEC), by incubating tag-free IgLON5 with Fab2513 for 1 h at 4 °C. Separation of the constructs showed that IgLON5 forms a dimer, as expected[13]. In contrast, IgLON5 in complex with Fab2513 eluted as a high–molecular weight complex of ~240 kDa, consistent with two Fabs bound to the IgLON5 dimer (**Fig. 2a** and **b)**.To confirm this findingand determinethe affinity of Fab2513 to IgLON5, we used biolayer interferometry (BLI). We immobilized Fab2513 at 100 nM on biosensor tips and probed for interaction with a solution of IgLON5 at varying concentrations (**Fig. 2c)**.We detected,a high affinity interaction between Fab2513 and IgLON5, with a calculated Kd value of $1.5\pm0.08\times10^{-12}$ M. To assess potential cross-reactivity of the mAb2513, we tested its binding on the other IgLON family members by ELISA. We observed a strong reactivity for IgLON5, but no binding could be detected for the other protein members, highlighting the mAb high specificity (**Supplementary Fig. 4)**. Given that purified IgG from patient sera have been shown to bind neuronal cell surfaces and induce IgLON5 clustering and internalization[26,30], we investigated the cellular binding of mAb2513 on human

induced pluripotent stem cell (hiPSC)-derived neurons[36]. We observed signal on cell bodies and dendrites (MAP2+) of neurons, while no signal was observed with an irrelevant antibody (palivizumab) confirming the mAb biological specificity (**Fig. 2d)**. To further investigate cell surface clustering, we used SH-SY5Y neuroblastoma cells transfected with either IgLON5 or IgLON4 and probed them with biotinylated recombinant IgLON5. The transfected cells were analysed by flow cytometry in the presence or absence of mAb2513 and we monitored geometric mean fluorescence intensity (gMFI) associated to the cell surface using fluorescent streptavidin. We observed a clear association of fluorescent biotinylated IgLON5 with IgLON4 transfected cells (gMFI : 166.9±1.0), and to lesser extend with IgLON5 transfected cells (gMFI: 19.03±1.3), an expected result because both proteins are known to form complexes[13,26] (**Fig. 2e** and **Supplementary Fig. 5)**. Interestingly, in the presence of mAb2513 fluorescence increased, with gMFI of 250.4±1.1 and 164.5±1.3 for IgLON4 and IgLON5, respectively (**Fig. 2e)**. In contrast, no fluorescence increased was observed in the presence of an irrelevant human mAb (palivizumab), nor in the presence of Fab2513. This result demonstrates that mAb2513 can bind IgLON5 homo- and heterodimers in *trans* and may thereby induce clustering on neuronal cell surface.

Cryo-EM structure of the IgLON5 dimer in complex with Fab2513

To define the molecular architecture of the complex, we performed single-particle cryo–electron microscopy and determined its structure at 3.7 Å resolution, estimated by Fourier shell correlation curves (FSC) (**Table 1, Supplementary Fig. 6** and **7**). The resulting cryo-EM map displayed higher-resolution features for the first two Ig-like domains (Ig1 and Ig2), whereas the third Ig-like domain (Ig3) was not resolved, likely due to pronounced interdomain flexibility, as previously reported[13] (**Fig. 3a)**. Structural analysis reveals that IgLON5 forms a homodimer in the complex, arranged in a head-to-head configuration via a common interface involving the first Ig-like (Ig1) domains. Interestingly, each Fab engages IgLON5 in an opposite orientation, with the epitopes positioned on opposing faces of the dimer (**Fig. 3a** and **b)**. This spatial arrangement demonstrates that the antibody cannot bind bivalently to a single IgLON5 dimer. Instead, the two Fab arms could engage epitopes on adjacent dimers, thereby promoting receptor clustering. This result is consistent with the mAb2513-induced multimerization of IgLON5 on the surface of SH-SY5Y cells and provides a mechanistic explanation for the previously reported clustering observed with patient-derived IgG on murine neurons[30,31]. The IgLON5 dimerization is mediated by the two Ig1 domains, which bury approximately 780 Å² of surface area per monomer and orient the two monomers at a 90° angle relative to each other (**Fig. 3b)**. The interface is stabilized by a dense and complementary combination of electrostatic, hydrogen-binding, and hydrophobic interactions distributed across the β-sheet faces and adjacent loop regions (**Fig. 3c** and **d)**. A prominent electrostatic anchor is formed by a salt bridge between D50 of one protomer and R35 of the reciprocal protomer andreinforced by additional polar van der Waals and weak hydrogen contacts (CH–O/N), establishing a strong interdomain constraint (**Fig. 3e)**. The R35 and W52 residues from one protomer form a central interaction hub, with W52 engaging R35 of the other protomer through CH–π interactions together with polar and apolar van der Waals contacts, while the R35 establishes multiple proximal contacts with I44, A47, and W52 creating a tightly packed core (**Fig. 3e)**. The central portion of the interface is enriched in

hydrophobic contacts. Reciprocal L39 and I44 form multiple proximal and apolar van der Waals interactions. These interactions generate a compact nonpolar interface that likely shields buried surfaces from solvent (**Fig. 3f)**. Surrounding this hydrophobic core, an extended polar network contributes to specificity and orientation. Notably, N43 forms a hydrogen bond with S86 and engages in additional CH–O/N and apolar contacts with P93 and T95 (**Fig. 3f)**. Reciprocally, S86 forms a hydrogen bond with S42, reinforcing the polar interaction network. Several additional proximal contacts involving S42, S54, Q88, and T95 with polar residues in domain I create an extended hydrogen-bond-compatible surface. Overall, the Ig1–Ig1 interface is characterized by a central aromatic–arginine interaction cluster, symmetric hydrophobic packing, and a peripheral web of hydrogen bonds and polar contacts. This combination of electrostatic anchoring, π-mediated interactions, and complementary van der Waals packing likely confers substantial rigidity to the Ig1 dimerization module. From a biological perspective, the rigid head-to-head dimerization, together with the observation that antibodies promote cross-linking of adjacent dimers rather than bivalent engagement of a single dimer, suggests that they primarily act by aberrantly clustering the receptor at the neuronal surface.

Characterization of Fab paratope and epitope

To investigate the epitope and paratope involved in the interaction, we performed local refinement of the EM map using a mask encompassing Fab2513 and the second Ig domain of IgLON5. The resulting map reached 3.5 Å resolution, allowing clear identification of the residues involved in the interaction (**Fig. 4a, Table 1, Supplementary Fig. 6** and **7**). The Fab adopts a pincer-like configuration to engage the second Ig domain of IgLON5, with the heavy and light chains clasping the domain from opposite sides (**Fig. 4b**). This interaction is mediated by a compact and highly complementary interface spanning residues 163–205 of IgLON5, burying a total surface area of 680 Å² (**Fig. 4c**). All three CDRs of the heavy chain and the third of the light chain are involved in binding. The VH provides the dominant contribution to binding with 620 $Å^2$ and establishes an extended network of polar and hydrophobic interactions across the Ig2 domain of IgLON5. The first CDR is strongly involved in the interaction accounting for half of the buried surface area, with four residues making specific bonds. The CDRH1-S32 (germline encoded) and CDRH1-N33 make hydrogen bounds with T163/T174, and T165/S175, respectively. The CDRH1-Y35, also encoded in the germline, interacts with L169, D171, F173, T174 and Q194 (**Fig. 4d)**. Within the CDRH2, residues Y52 (germline encoded) and F53 interact with V196 and H198, while Y58 (germline encoded) forms a contact with R167 (**Fig. 4e)**. The CDRH3 forms a central interaction network involving CDRH3-N97, which forms non-conventional H-bonds (CH–O/N), interactions with G172, F173 and additional contacts with T174. The CDRH3-R98 and M99 further stabilize this region through CH–O/N and van der Waals interactions with F173 and T174, while F173 is also engaged in apolar contacts with CDRH3-M99 (**Fig. 4f)**. Surrounding this polar core, extensive hydrophobic and proximal contacts reinforce the interface, particularly around the G172, F173 and T174 segment (**Fig. 4g)**. The aromatic and aliphatic residues from CDRH1-Y35, CDRH2-Y52, F53, and CDRH3-M99, F00 pack against W166, R167, Q168, L169, D171, L180, Q181, I182, Q189, Y193, V196, H198, and P205, creating a tightly interlocked and shape-complementary surface (**Fig. 4h)**. The light chain plays a supportive but significant role by reinforcing the same epitope hotspot. CDRL3-Y91 forms a hydrogen bond with D171 and establishes

proximal contacts with G172, while CDRL3-T93 contributes additional interactions with D171, complementing the heavy-chain hydrogen-bond network and stabilizing the central binding region. Despite the high structural homology within the IgLON family, mAb2513 does not exhibit cross-reactivity with other members. To explore the molecular basis of this specificity, we aligned the amino acid sequences of the different IgLON proteins. We observed that antibody binding is centered on the highly variable (β12–β12') loop, which represents the most divergent region among IgLON family members **(Supplementary Fig. 8).** Our structural data indicate that the interaction is predominantly mediated by germline-encoded residues, as seven of ten unmutated residues in CDRH1 and CDRH2 directly contribute to the binding interface. This finding suggests that IgLON5 recognition is largely driven by germline-encoded features, raising the possibility that autoreactive antibodies can emerge from the naïve repertoire with limited affinity maturation. Our results further indicate that Fab binding does not sterically hinder IgLON5 homo-interactions or heterodimer formation but instead may stabilize pre-existing dimers and promote higher-order multimerization through cross-linking of adjacent IgLON5 molecules. Thus, the structural organization of IgLON5 and the spatial orientation of its extracellular domains support a model in which antibody binding is fully compatible with, and may even facilitate, IgLON5 clustering at the plasma membrane, consistent with the IgLON5 and IgLON4 crosslinking observed in the presence of the mAb.

Discussion

An increasing number of central nervous system disorders are now recognized as antibody-mediated diseases characterized by autoantibodies directed against extracellular domains of neuronal or glial surface antigens[37,38]. These autoantibodies can directly interfere with protein function, alter synaptic signalling, or induce receptor internalization, leading to neuronal dysfunction[22,38]. Unlike classical paraneoplastic syndromes targeting intracellular antigens, these conditions are frequently responsive to immunotherapy, highlighting their primarily antibody-mediated pathogenic mechanisms. Among them, anti-IgLON5 disease is unique in that it lies at the interface between autoimmunity and neurodegeneration and therefore entails an additional layer of complexity[18]. Understanding the provenance, repertoire and serological consequences of anti-IgLON5 B cells is essential for delineating the pathogenesis of the disease and for therapeutic insights. However, most previous studies have relied on polyclonal IgG purified from patient sera, limiting the ability to dissect antigen specificity at the monoclonal level.

Here, we report, the first sequence and high-resolution structure of a human monoclonal antibody binding IgLON5 with high affinity, providing direct insight into the molecular basis of antigen recognition in this disease. At the repertoire level, our analysis indicates that the anti-IgLON5 response in this patient is polyclonal, with no evidence of dominant clonal expansion. This response may arise through bystander T cell activation, engagement of Toll-like receptors in a proinflammatory B cell environment or through widespread activation of diverse B cell clones by foreign or self-antigen[39]. The identification of a modest, but statistically significant increase in somatic hypermutation frequency compared to healthy

donors might suggest that high affinity anti-IgLON5 antibodies derive from a sustained antigen stimulation, a finding also in agreement with the predominance of IgG4 observed[23]. Among the identified clones, one IgG4 antibody using the IGHV4-39 germline gene was selected for structural and functional characterization. The IGHV4-39 gene has been recurrently associated with autoreactive antibodies in systemic autoimmune diseases such as systemic lupus erythematosus, antiphospholipid syndrome, and multiple sclerosis[40-42]. Thus, suggesting that intrinsic features of this germline gene may predispose certain B cell clones toward self-reactivity. However, the absence of marked clonal expansion indicates that autoreactivity in anti-IgLON5 disease is unlikely to arise from a single dominant lineage and may instead contribute to the clinical heterogeneity observed across patients.

The structural analysis reveals that the antibody recognizes a conformational epitope located within the second Ig-like domain of IgLON5. This mode of binding highlights the importance of native protein folding in antibody recognition and is consistent with the absence of reactivity observed against other members of the IgLON family despite their high degree of structural homology[9,43]. Sequence comparison indicates that the antibody footprint overlaps with the loop (β12–β12') of the Ig2 domain, one of the most divergent regions among IgLON proteins, supporting the idea that subtle structural variations within surface-exposed loops drive antigen specificity. These findings provide a molecular explanation for the selective targeting of IgLON5 and reinforce the notion that autoimmune responses against neuronal surface proteins can achieve high specificity despite conserved protein architectures.

The Fab engages the Ig2 domain of each protomer in an antiparallel manner within the IgLON5 dimer, recapitulating observations previously reported with purified patient IgG[31]. Notably, our data demonstrate that Fab binding does not disrupt the IgLON5 dimerization interface but instead promotes higher-order homo- or hetero-multimerization. Such antibody-induced clustering has been reported to trigger receptor internalization and may contribute to neuronal dysfunction and tau pathology[30].The paratope involves all three CDRs of the heavy chain and CDR3 of the light chain, with interactions mediated in part by germline-encoded residues within CDRH1 and CDRH2. This observation suggests that germline features play a key role in antigen recognition and may predispose this antibody toward binding self-antigens. Consistent with this notion, low-affinity binding of self-antigens by germline BCR has recently been shown to be an essential step in the generation of anti-NMDAR antibodies in human breast cancer[44].

Our study has some limitations, the structural and functional analyses are based on a mAb derived from a single patient, and it remains to be determined whether similar epitopes and binding modes are shared across individuals. In addition, while our data provide a structural framework for understanding antibody binding, the downstream cellular consequences of this interaction require further investigation. Future studies should aim to characterize additional mAbs from multiple patients to assess the degree of convergence in epitope targeting and germline usage. Finally, integrating structural insights with in vivo models may help clarify how antibody-mediated perturbations of IgLON5 translate into the complex clinical phenotype of the disease.

In conclusion, our work provides the first high-resolution view of a human monoclonal antibody targeting IgLON5 and reveals a mechanism of antigen recognition that preserves IgLON5 dimerization while likely altering its organization at the cell surface. This reorganization may contribute to downstream pathogenic effects, such as tau phosphorylation, missorting, and over time tau deposition and neurodegeneration. These findings not only redefine current models of pathogenicity in anti-IgLON5 disease and support a paradigm in which antibody-mediated functional modulation, rather than direct structural disruption, drives neuronal dysfunction in autoimmune disorders of the central nervous system.

Materials and Methods

Patient and sample description

PBMCs were obtained from a 60-year-old male diagnosed with anti-IgLON5 disease. The patient presented a 7-year history of sleep disturbances characterized by abnormal nocturnal movements and behaviors, mild sleep-onset and maintenance insomnia, and severe daytime somnolence with episodes of unintended sleep. During sleep, he exhibited loud snoring, frequent vocalizations, groaning, and complex motor behaviors, including punching, kicking, jerking, and gesturing. Additional neurological symptoms included mild dysphagia with occasional choking episodes, gait unsteadiness with infrequent falls, and persistent daytime motor restlessness. Neurological examination showed distal choreic movements affecting the upper and lower limbs and abnormal postural reflexes on the pull test. Overnight video-polysomnography was performed and demonstrated a NREM and REM parasomnia with stridor and severe obstructive sleep apnea (apnea–hypopnea index: 44 events/hour). Laryngoscopic evaluation revealed mild bilateral vocal cord paresis. Routine blood tests, cerebrospinal fluid analysis, and brain MRI were unremarkable. IgLON5 antibodies, however, were detected in both serum and cerebrospinal fluid, confirming the diagnosis of anti-IgLON5 disease. HLA typing was positive for the *DRB1*10:01 and DQB1*05:01* haplotype. The patient received immunotherapy with high-dose intravenous corticosteroids followed by rituximab, without clinical improvement. Continuous positive airway pressure therapy effectively eliminated stridor and obstructive sleep apnea and improved daytime sleepiness, while abnormal sleep-related movements and behaviors persisted. The patient repertoire comprised 3.1% IgG1, 4.1% IgG2, 1.1% IgG3, and 0.5% IgG4 of IgLON5 specific clones. Written informed consent for the storage and research use of PBMC sample was obtained from the patient. The study was approved by the ethics committee of Hospital Clínic (2018-0336 ER-01), Barcelona, Spain.

Cell Lines

Expi293F cells (ThermoFisher, Cat No# A14527), a human embryonic kidney cell line adapted for suspension growth, were obtained from Thermo Fisher Scientific and cultured in Expi293 Expression Medium (Gibco, Cat No #A1435101) and HyCell TransFx-H liquid medium (Cytiva, Cat No. #SH30939.02) Supplemented with GlutaMax (Gibco, Cat No #10860311), Sodium pyruvate (ThermoFisher, Cat No# 11360070), and Poloxamer 188 (Gibco, Cat No #24040032). SH-SY5Y cells, a human neuroblastoma cell

line, were obtained from ATCC (CRL-2266) and cultured in a 1:1 mixture of ATCC-formulated Eagle's Minimum Essential Medium (ATCC, 30-2003) and F-12 Medium (Gibco, Thermo Fisher Scientific, #11765054), supplemented with 10% FBS (Sigma-Aldrich).

Staining of hiPSC-derived neurons

Neurons were obtained through differentiation of human induced pluripotent stem cell (hiPSC)-derived neural precursor cells (NPCs) and characterized, as previously described (cell line ID: LNISi002 -B)[36,45]. To assess both extracellular and intracellular mAb binding to hiPSC-derived neurons, cells were fixed with 3% paraformaldehyde (PFA), 0.1% glutaraldehyde, and 2% sucrose for 10 minutes at room temperature (RT), followed by staining as previously described[46]. Briefly, after permeabilization and blocking of non-specific binding sites using a permeabilization/blocking buffer (Perm./Block buffer: 5% normal goat serum (Jackson ImmunoResearch), 0.2% saponin, and 0.1% Triton X-100 (Sigma-Aldrich) in PBS) cells were incubated overnight at 4°C with either anti-MAP2 (Abcam), anti-IgLON-5 (5 µg/mL) or Palivizumab (isotype control; 5 µg/mL), all antibodies diluted in Perm./Block buffer. Subsequently, biotinylated human anti-IgG secondary antibodies (Invitrogen, 31774; 1:100) were applied for 30 minutes at RT to detect bound primary antibodies. Following extensive PBS washes, phycoerythrin (PE)-labeled streptavidin (BD, Cat No#554061) was added and incubated for 30 minutes at RT. Cells were then counterstained with 4',6-diamidino-2-phenylindole (DAPI, Sigma-Aldrich) diluted in PBS for 10 minutes at RT. All samples and controls were performed in duplicates. Fluorescence microscopy of stained cells was automated using a high-performance EVOS M7000 imaging system. Four images were acquired per well. Post-acquisition image processing was performed using ImageJ software (NIH, v1.52t). Image acquisition and processing were conducted using identical parameters for specific antibodies and corresponding controls.

Cell sorting

PBMCs were stained on ice for 20 min with the following fluorochrome-labelled mouse monoclonal antibodies: CD3-APC/Cy7 (clone HIT3a, Cat No#300317, BioLegend), CD20-PE-Cy7 (clone L27, Cat No#335793, BD Biosciences), and anti-human IgD PE-CF594 (BD Biosciences; Cat No#562540; Clone IA6-2). Cells were sorted to over 98% purity on a FACS Aria III (BD) using the following gating strategy: circulating memory B cells were sorted as CD3–, CD20+ IgD-, IgLON5 labelled with Alexa647+/-. The FACS-sorted B cells were collected in 6µl FCS in Eppendorf tubes that were pre-coated overnight with BSA (Sigma-Aldrich).

IgLON clustering assay

Biotinylated IgLON5 was preincubated for 15 minutes on ice with Streptavidin-PE (ThermoFisher, Cat No#12-4317-87), then mAbs (Isotype control (palivizumab) or mAb2513) or Fab2513 were added to the reaction for 5-10 minutes on ice, before addition to the cells. Clustering on the cells surface was analysed by flow cytometric in presence of LIVE/DEAD fixable Violet Dead Cell Stain (ThermoFisher,

Cat No#L34964). Geometric mean fluorescence intensity (gMFI) was quantified using BD FACSDiva and subsequently analysed and plotted in GraphPad Prism (v10.4.1).

Single-cell BCR-seq library preparation and sequencing

Single-cell 5' V(D)J libraries were generated using Chromium Next GEM Single Cell V(D)J Reagent kit v3 (10X Genomics) according to the manufacturer's protocol. Paired heavy and light chain BCR libraries were prepared from the sorted B cell populations. Briefly, up to 20,000 memory B cells per well of 10X chip were loaded in the 10X Genomics Chromium Controller to generate single-cell gel beads in emulsion. After reverse transcription, gel beads in emulsion were disrupted. Barcoded complementary DNA was isolated and used for the preparation of BCR libraries. All steps were performed according to the manufacturer's instructions. The purified libraries from four biological replicates of donor D1 (one IgLON5 positive and three negative) were pooled separately and sequenced on the Element AVITI System as per the instructions provided in 10X Genomics user guide for the read length and depth.

Paired BCR repertoire

V(D)J annotation was performed using cellranger vdj (v10.0) on each sample individually, after which sequences and annotations were pooled into a single filtered_contig.fasta and filtered_contig_annotations.csv file for downstream processing within the Immcantation framework (http://immcantation.org; Change-O v1.3.0)[47]. Sequences were subsequently annotated using IgBLAST v1.22[48] against the IMGT database[49] (accessed 8 December 2025). Only productive rearrangements were retained, and heavy and light chain sequences were separated into independent files prior to clonal analysis[50]. Clone assignment was performed using the Change-O DefineClones function, grouping sequences by IGHV gene, IGHJ gene, and junction sequence similarity (distance threshold = 0.15). Clone definitions were subsequently verified and corrected using the light_cluster function, which leverages light chain pairing information associated with each heavy chain clone. Germline sequences were reconstructed using the CreateGermlines function, and sequences harboring incomplete V(D)J rearrangements or in-frame stop codons were excluded from further analysis. For downstream repertoire analysis, only heavy chains paired with exactly one κ or one λ light chain were retained. The filtered heavy and light chain sequences were concatenated into a single AIRR format file for use as input for scRepertoire v6.2.2[51]. The same pipeline was applied to two publicly available healthy donor datasets[33].The three repertoires yielded 9,577 paired BCRs for D1 (IgLON5 patient), 7,263 for H1, and 7,539 for H2. Clonal diversity was assessed using coverage-based rarefaction and extrapolation analysis, implemented via the clonalRarefaction() function from scRepertoire. Sample completeness curves were first generated to evaluate the relationship between the number of sequenced cells and sample coverage for each donor (plot.type = 2). Coverage-based rarefaction curves were then computed for two Hill diversity orders: species richness (Hill q = 0), which accounts for clonal richness alone, and Shannon diversity (Hill q = 1), which incorporates both clonal richness and evenness (plot.type = 3). For all metrics, rarefaction (interpolation) was performed up to the observed sample size, and extrapolation

was extended beyond it. Confidence intervals were estimated using bootstrap resampling (95% CI, n.boots = 50). V gene usage was visualized using the vizGenes() function from scRepertoire. Mutation frequency was calculated as the number of residue differences between the BCR protein sequence and its inferred germline sequence across the FWR1, CDR1, FWR2, CDR2, and FWR3 regions of the VH gene. Clonal network of CDRH3 sequences was constructed using the clonalCluster() function from scRepertoire v2.2.1. Briefly, clonal family identifiers derived from the Immcantation workflow were used as V gene input, replacing the VH gene in the CTgene metadata, for edit-distance-based clustering (parameters: chain = "IGH", sequence = "aa", threshold = 0.81). Statistics were conducted using R Statistical Software (v4.4.1).

Recombinant antibody production

Expi293 cells (Thermo Fisher, Cat. No. A14527) were diluted to a cell density of 2.5 × 10^6 cells/mL in cell culture medium. Heavy chain and light chain plasmids were complexed with Polyethyleneimine (ThermoFisher) and added to the cells. On day five, cells were cleared from cell culture media by centrifugation at 10,000*g* for 30 min and subsequently passed through a 0.22-µm filter. The supernatant containing the recombinant antibody was applied on protein A resin (Cytiva) at 4 °C. The resin was washed with 10 column volumes (CV) of phosphate-buffered saline (PBS) and antibody eluted with 3 CV of 100 mM glycine pH 2.9[52]. The acidic pH of the eluted antibody solution was increased to approximately 7 by the addition of 1M Tris pH 8.0. The antibody solution was buffer exchanged into PBS with successive rounds of centrifugation, filtered, and stored at −80 °C.

Fragment antigen binding (Fab) generation

For Fab production, the heavy chain was engineered at the hinge region to include a two–amino acid glycine–serine linker, followed by a C-terminal six-histidine tag and a stop codon. Light and mutated heavy chains were transfected as described in the previous section. Cell supernatant was harvested five- or six-days post transfection and purified by IMAC chromatography, followed by size exclusion chromatography on a Superdex 200 Increase 10/300 GL column.

Recombinant proteins production

DNA encoding either the full length ORFs or truncated version of IgLON proteins (residues 1–316) fused to human IgG1 Fc domain or a linker followed by tandem Strep tag and 6×His tag were ordered from Twist Bioscience (sequence of construct are listed in **Supplementary Fig. 9**). The plasmids were transfected into Expi293 cells using polyethyleneimine (ThermoFisher) as described above. The recombinant proteins were purified by either IMAC or Protein A affinity chromatography, followed by digestion with immobilized papain agarose (Thermo Fisher Scientific) to remove the Fc fragment. The cleaved IgLON were further purified by size-exclusion chromatography on a 200 Increase 10/300 GL column (Cytiva). Fractions containing the IgLON proteins were pooled, sterile-filtered, snap-frozen, and stored at −80 °C.

Biolayer interferometry

The biolayer interferometry experiments using IgLON5 were performed as follows. All experiments were performed in reaction buffer (PBS pH 7.4 + 0.01% (w/v) BSA + 0.002% (v/v) Tween 20) at room temperature (RT) using an Octet K2 instrument (ForteBio). FAB2G (Fortebio) biosensor probes were first equilibrated in reaction buffer for 600 s. Fab fragments were diluted to 5 µg/ml in reaction buffer and immobilized onto the FAB2G probes for 600 s, followed by a wash for 300 s in reaction buffer. The binding of IgLON5 to the Fab was then measured at various concentrations for 400 s, followed by dissociation for 500 s in reaction buffer. Analysis was performed using the Octet software and GraphPad Prism version 9.0.

Cryo-EM sample preparation

IgLON5/Fab complexes were prepared using a stock solution at 2 mg/ml by incubating IgLON5 protein with a tree-fold molar excess of Fab2315. To prevent interaction of the complex with the air-water interface during vitrification, the sample was incubated with 0.005% (w/v) fluorinated Fos-Choline 8 (FC8) (Thermo Fisher Scientific). Next, sample was applied to plasma cleaned Quantifoil 1.2/1.3 300 -mesh Cu holey carbon grids (Electron Microscopy Sciences). The grid was blotted in an automatic plunge freezing apparatus Vitrobot MarkIV (Thermo Fisher, Hillsboro, USA) to control humidity and temperature[50].

Cryo-EM data collection

Grids were screened for particle presence and ice quality on a TFS Glacios microscope (200 kV), and the best grids were transferred to a TFS Titan Krios G4. Cryo-EM data were collected using a TFS Titan Krios G4 transmission electron microscope, equipped with a Cold-FEG on a Falcon IV detector in electron counting mode. Falcon IV gain references were collected just before data collection. Data were collected using TFS EPU v2.12.1 utilizing the aberration-free image shift protocol, recording 4 micrographs per ice hole. Movies were recorded at a magnification of ×81,000, corresponding to the 0.83 Å pixel size at the specimen level, with defocus values ranging from −1.2 to −2.4 µm. Exposures were obtained with 17.34 e^{-} $Å^{-2}$ s dose, resulting in an exposure time of approximately 2.75 s per movie. In total, 17,169 micrographs in EER format were collected.

Cryo-EM Data processing and structure fitting

Data processing was performed with cryoSPARC V4.4 including motion correction and CTF determination[53]. Initial particle picking was performed using blob picking on 1,000 micrographs. The extracted particles were sorted by 2D classification, and the

resulting classes were used to train DeepPicker, which was then applied to the full dataset[54]. Particles extraction (box size 448 pixels^2) was carried out using cryoSPARC[53]. Next, several rounds of reference-free 2D classification were performed to remove artifacts and selected particles were used for ab-initio reconstruction and hetero-refinement. After hetero-refinement, 702'836 particles contributed to an initial 3D reconstruction of 3.7 Å resolution (FSC 0.143) with C1 symmetry. Local refinement was performed with mask generated with UCSF Chimera around IgLON5 domain 2 and Fab and generated a map at 3.5 Å resolution. The model of a IgLON5 dimer (PDB ID: 6DLE)[13] and model of Fab 2315 (obtained withAlphaFold2[55]) were fitted into the cryo-EM maps with UCSF Chimera. These docked models were extended and rebuilt manually with refinement, using Coot and Phenix[56,57]. Figures were prepared in UCSF Chimera, UCSF ChimeraX and Pymol[58]. The numbering of Fab 2315 is based on Kabat numbering of immunoglobulin models[59]. Buried surface area measurements were calculated within ChimeraX and PISA[60].

Statistical analysis

Statistics were conducted using R Statistical Software (v4.4.2) and with Prism Graph Pad (v10) using one-way ANOVA with Tukey's multiple comparisons test.

Declarations

Data and code availability

The associated scripts are available on https://github.com/MathildeFogPerez/manuscript-iglon5-D1. Raw sequencing data files for single-cell VDJ sequencing are available at ENA database: PRJEB109754. Processed data files (BCR repertoires) are available at Zenodo: https://doi.org/10.5281/zenodo.18925481. Cryo-EM map and PDB Model were deposited on EMDB: and PDB with the following accession numbers EMD-57080 and EMD-57198 with PDB-ID:29CP and PDB-ID: 29IN

Funding

This study was supported in part by funding from the Swiss National Science Foundation awarded to L.P (Grant number: 10005403).

Acknowledgements

We thank the patient for his willingness to donate blood samples for this study. The authors acknowledge Dr. Francesc Graus for study input and critical review of the manuscript. We thank Claire Aubert for preliminary experiments involving IgLON5 clustering. We acknowledge the Lausanne Genomic Technologies Facility (UNIL) for next-generation sequencing of the samples. We thank the Dubochet Center for Imaging (an EPFL, UNIGE, UNIL initiative), and particularly Dr. Emiko Uchikawa, for cryo-EM grid preparation and data collection.

Author contributions

A.R., R.S., and D.V.S., expressed and purified proteins. A.R., D.V.S., and A.L., performed cell staining and sorting. R.R.W. performed IgLON5 and Fab expression, purification, characterization, and validation. A.R., I.S., and A.M. performed and analysed experiments with neurons. L.S., R.D., C.G., J.D., and F.G. provided critical samples or reagents. M.F. performed and analysed immune repertoire data. L.P. conceived the study and supervised the project. M.F. and L.P. wrote the manuscript, with input from the other authors.

Competing interests

The authors declare no competing interest.

References

1. Singh, K. *et al.* The IgLON family of cell adhesion molecules expressed in developing neural circuits ensure the proper functioning of the sensory system in mice. *Scientific reports* **14**, 22593 (2024). https://doi.org:10.1038/s41598-024-73358-z
2. Apóstolo, N. *et al.* Synapse type-specific proteomic dissection identifies IgSF8 as a hippocampal CA3 microcircuit organizer. *Nature communications* **11**, 5171 (2020). https://doi.org:10.1038/s41467-020-18956-x
3. Sanz, R., Ferraro, G. B. & Fournier, A. E. IgLON Cell Adhesion Molecules Are Shed from the Cell Surface of Cortical Neurons to Promote Neuronal Growth*. *Journal of Biological Chemistry* **290**, 4330-4342 (2015). https://doi.org:https://doi.org/10.1074/jbc.M114.628438
4. Hashimoto, T., Maekawa, S. & Miyata, S. IgLON cell adhesion molecules regulate synaptogenesis in hippocampal neurons. *Cell Biochemistry and Function* **27**, 496-498 (2009). https://doi.org:https://doi.org/10.1002/cbf.1600
5. Marg, A. *et al.* Neurotractin, a novel neurite outgrowth-promoting Ig-like protein that interacts with CEPU-1 and LAMP. *The Journal of cell biology* **145**, 865-876 (1999). https://doi.org:10.1083/jcb.145.4.865

6. Schäfer, M., Bräuer, A. U., Savaskan, N. E., Rathjen, F. G. & Brümmendorf, T. Neurotractin/kilon promotes neurite outgrowth and is expressed on reactive astrocytes after entorhinal cortex lesion. *Molecular and cellular neurosciences* **29**, 580-590 (2005). https://doi.org:10.1016/j.mcn.2005.04.010
7. Pischedda, F. *et al.* A Cell Surface Biotinylation Assay to Reveal Membrane-associated Neuronal Cues: Negr1 Regulates Dendritic Arborization*. *Molecular & Cellular Proteomics* **13**, 733-748 (2014). https://doi.org:https://doi.org/10.1074/mcp.M113.031716
8. Salluzzo, M. *et al.* The Role of IgLON Cell Adhesion Molecules in Neurodegenerative Diseases. *Genes (Basel)* **14** (2023). https://doi.org:10.3390/genes14101886
9. Venkannagari, H. *et al.* Highly Conserved Molecular Features in IgLONs Contrast Their Distinct Structural and Biological Outcomes. *Journal of molecular biology* **432**, 5287-5303 (2020). https://doi.org:10.1016/j.jmb.2020.07.014
10. Kubick, N., Brösamle, D. & Mickael, M.-E. Molecular Evolution and Functional Divergence of the IgLON Family. *Evolutionary Bioinformatics* **14**, 1176934318775081 (2018). https://doi.org:10.1177/1176934318775081
11. McNamee, C. J., Youssef, S. & Moss, D. IgLONs form heterodimeric complexes on forebrain neurons. *Cell Biochem Funct* **29**, 114-119 (2011). https://doi.org:10.1002/cbf.1730
12. Reed, J., McNamee, C., Rackstraw, S., Jenkins, J. & Moss, D. Diglons are heterodimeric proteins composed of IgLON subunits, and Diglon-CO inhibits neurite outgrowth from cerebellar granule cells. *Journal of cell science* **117**, 3961-3973 (2004). https://doi.org:10.1242/jcs.01261
13. Ranaivoson, F. M. *et al.* A Proteomic Screen of Neuronal Cell-Surface Molecules Reveals IgLONs as Structurally Conserved Interaction Modules at the Synapse. *Structure* **27**, 893-906.e899 (2019). https://doi.org:10.1016/j.str.2019.03.004
14. Mialon, M. *et al.* A trans-synaptic IgLON adhesion molecular complex directly contacts and clusters a nicotinic receptor. *Nature communications* **17**, 1404 (2026). https://doi.org:10.1038/s41467-025-68141-1
15. Sabater, L. *et al.* A novel non-rapid-eye movement and rapid-eye-movement parasomnia with sleep breathing disorder associated with antibodies to IgLON5: a case series, characterisation of the antigen, and post-mortem study. *Lancet Neurol* **13**, 575-586 (2014). https://doi.org:10.1016/s1474-4422(14)70051-1
16. Gaig, C. *et al.* Clinical manifestations of the anti-IgLON5 disease. *Neurology* **88**, 1736-1743 (2017). https://doi.org:10.1212/WNL.0000000000003887
17. Höllerhage, M. *et al.* Transcriptome and Proteome Analysis in LUHMES Cells Overexpressing Alpha-Synuclein. *Frontiers in Neurology* **Volume 13 - 2022** (2022). https://doi.org:10.3389/fneur.2022.787059
18. Reinecke, R. *et al.* Brainstem pathology in anti-IgLON5 disease: new insights into early events and tau progression. *Brain* (2026). https://doi.org:10.1093/brain/awag015
19. Gelpi, E. *et al.* Neuropathological spectrum of anti-IgLON5 disease and stages of brainstem tau pathology: updated neuropathological research criteria of the disease-related tauopathy. *Acta*

neuropathologica **148**, 53 (2024). https://doi.org:10.1007/s00401-024-02805-y

20. Yogeshwar, S. M. *et al.* HLA-DQB1*05 subtypes and not DRB1*10:01 mediates risk in anti-IgLON5 disease. *Brain* **147**, 2579-2592 (2024). https://doi.org:10.1093/brain/awae048
21. Werner, J. *et al.* Anti-IgLON5 Disease: A New Bulbar-Onset Motor Neuron Mimic Syndrome. *Neurol Neuroimmunol Neuroinflamm* **8** (2021). https://doi.org:10.1212/nxi.0000000000000962
22. de Bruijn, M. *et al.* Autoimmune encephalitis. *Nat Rev Dis Primers* **11**, 65 (2025). https://doi.org:10.1038/s41572-025-00650-1
23. Rispens, T. & Huijbers, M. G. The unique properties of IgG4 and its roles in health and disease. *Nature Reviews Immunology* **23**, 763-778 (2023). https://doi.org:10.1038/s41577-023-00871-z
24. Gaig, C. *et al.* Frequency and Characterization of Movement Disorders in Anti-IgLON5 Disease. *Neurology* **97**, e1367-e1381 (2021). https://doi.org:doi:10.1212/WNL.0000000000012639
25. Grüter, T. *et al.* Clinical, serological and genetic predictors of response to immunotherapy in anti-IgLON5 disease. *Brain* **146**, 600-611 (2022). https://doi.org:10.1093/brain/awac090
26. Landa, J. *et al.* Patients' IgLON5 autoantibodies interfere with IgLON5-protein interactions. *Frontiers in immunology* **Volume 14 - 2023** (2023). https://doi.org:10.3389/fimmu.2023.1151574
27. Sabater, L., Planagumà, J., Dalmau, J. & Graus, F. Cellular investigations with human antibodies associated with the anti-IgLON5 syndrome. *Journal of neuroinflammation* **13**, 226 (2016). https://doi.org:10.1186/s12974-016-0689-1
28. Landa, J. *et al.* Effects of IgLON5 Antibodies on Neuronal Cytoskeleton: A Link between Autoimmunity and Neurodegeneration. *Ann Neurol* **88**, 1023-1027 (2020). https://doi.org:10.1002/ana.25857
29. Gelpi, E. *et al.* Neuropathological criteria of anti-IgLON5-related tauopathy. *Acta neuropathologica* **132**, 531-543 (2016). https://doi.org:10.1007/s00401-016-1591-8
30. Askin, B. *et al.* IgLON5 autoimmune antibodies activate Tau via neuronal hyperactivity. *bioRxiv*, 2024.2003.2010.584272 (2025). https://doi.org:10.1101/2024.03.10.584272
31. Sabater, L., Planagumà, J., Dalmau, J. & Graus, F. Cellular investigations with human antibodies associated with the anti-IgLON5 syndrome. *Journal of neuroinflammation* **13**, 226 (2016). https://doi.org:10.1186/s12974-016-0689-1
32. Arendt, T., Stieler, J. T. & Holzer, M. Tau and tauopathies. *Brain research bulletin* **126**, 238-292 (2016). https://doi.org:10.1016/j.brainresbull.2016.08.018
33. Phad, G. E. *et al.* Clonal structure, stability and dynamics of human memory B cells and circulating plasmablasts. *Nature immunology* **23**, 1076-1085 (2022). https://doi.org:10.1038/s41590-022-01230-1
34. Ambegaonkar, A. A., Holla, P., Dizon, B. L. P., Sohn, H. & Pierce, S. K. Atypical B cells in chronic infectious diseases and systemic autoimmunity: puzzles with many missing pieces. *Current Opinion in Immunology* **77**, 102227 (2022). https://doi.org:https://doi.org/10.1016/j.coi.2022.102227

35. Bashford-Rogers, R. J. M., Smith, K. G. C. & Thomas, D. C. Antibody repertoire analysis in polygenic autoimmune diseases. *Immunology* **155**, 3-17 (2018). https://doi.org:10.1111/imm.12927
36. Perriot, S. *et al.* Neuron-reactive KIR+CD8+ T cells display an encephalitogenic transcriptional program in autoimmune encephalitis. *Nature communications* **16**, 8568 (2025). https://doi.org:10.1038/s41467-025-63573-1
37. Sun, B., Ramberger, M., O'Connor, K. C., Bashford-Rogers, R. J. M. & Irani, S. R. The B cell immunobiology that underlies CNS autoantibody-mediated diseases. *Nature Reviews Neurology* **16**, 481-492 (2020). https://doi.org:10.1038/s41582-020-0381-z
38. Prüss, H. Autoantibodies in neurological disease. *Nature Reviews Immunology* **21**, 798-813 (2021). https://doi.org:10.1038/s41577-021-00543-w
39. Bernasconi, N. L., Traggiai, E. & Lanzavecchia, A. Maintenance of serological memory by polyclonal activation of human memory B cells. *Science* **298**, 2199-2202 (2002). https://doi.org:10.1126/science.1076071
40. Bashford-Rogers, R. J. M. *et al.* Analysis of the B cell receptor repertoire in six immune-mediated diseases. *Nature* **574**, 122-126 (2019). https://doi.org:10.1038/s41586-019-1595-3
41. Dieudonné, Y. *et al.* Defective germinal center selection results in persistence of self-reactive B cells from the primary to the secondary repertoire in Primary Antiphospholipid Syndrome. *Nature communications* **15**, 9921 (2024). https://doi.org:10.1038/s41467-024-54228-8
42. von Büdingen, H. C. *et al.* B cell exchange across the blood-brain barrier in multiple sclerosis. *J Clin Invest* **122**, 4533-4543 (2012). https://doi.org:10.1172/jci63842
43. Venkannagari, H. *et al.* Highly Conserved Molecular Features in IgLONs Contrast Their Distinct Structural and Biological Outcomes. *Journal of molecular biology* **432**, 5287-5303 (2020). https://doi.org:https://doi.org/10.1016/j.jmb.2020.07.014
44. Kleeman, S. O. *et al.* Ectopic NMDAR expression in cancer unmasks germline-encoded autoimmunity. *Nature* (2026). https://doi.org:10.1038/s41586-026-10278-0
45. Mathias, A. *et al.* Human stem cell-derived neurons and astrocytes to detect novel auto-reactive IgG response in immune-mediated neurological diseases. *Frontiers in immunology* **15**, 1419712 (2024). https://doi.org:10.3389/fimmu.2024.1419712
46. Mathias, A. *et al.* Human stem cell–derived neurons and astrocytes to detect novel auto-reactive IgG response in immune-mediated neurological diseases. *Frontiers in immunology* **15** (2024). https://doi.org:10.3389/fimmu.2024.1419712
47. Foglierini, M. *et al.* RAIN: machine learning-based identification for HIV-1 bNAbs. *Nature communications* **15**, 5339 (2024). https://doi.org:10.1038/s41467-024-49676-1
48. Ye, J., Ma, N., Madden, T. L. & Ostell, J. M. IgBLAST: an immunoglobulin variable domain sequence analysis tool. *Nucleic acids research* **41**, W34-W40 (2013). https://doi.org:10.1093/nar/gkt382
49. Giudicelli, V. *et al.* IMGT/LIGM-DB, the IMGT® comprehensive database of immunoglobulin and T cell receptor nucleotide sequences. *Nucleic acids research* **34**, D781-D784 (2006). https://doi.org:10.1093/nar/gkj088

50. Foglierini, M., Pappas, L., Lanzavecchia, A., Corti, D. & Perez, L. AncesTree: An interactive immunoglobulin lineage tree visualizer. *PLoS computational biology* **16**, e1007731 (2020). https://doi.org:10.1371/journal.pcbi.1007731
51. Yang, Q., Safina, K. R., Nguyen, K. D. Q., Tuong, Z. K. & Borcherding, N. scRepertoire 2: Enhanced and efficient toolkit for single-cell immune profiling. *PLoS computational biology* **21**, e1012760 (2025). https://doi.org:10.1371/journal.pcbi.1012760
52. Perotti, M., Marcandalli, J., Demurtas, D., Sallusto, F. & Perez, L. Rationally designed Human Cytomegalovirus gB nanoparticle vaccine with improved immunogenicity. *PLOS Pathogens* **16**, e1009169 (2021). https://doi.org:10.1371/journal.ppat.1009169
53. Punjani, A., Rubinstein, J. L., Fleet, D. J. & Brubaker, M. A. cryoSPARC: algorithms for rapid unsupervised cryo-EM structure determination. *Nature methods* **14**, 290-296 (2017). https://doi.org:10.1038/nmeth.4169
54. Wang, F. *et al.* DeepPicker: A deep learning approach for fully automated particle picking in cryo-EM. *Journal of structural biology* **195**, 325-336 (2016). https://doi.org:https://doi.org/10.1016/j.jsb.2016.07.006
55. Jumper, J. *et al.* Highly accurate protein structure prediction with AlphaFold. *Nature* **596**, 583-589 (2021). https://doi.org:10.1038/s41586-021-03819-2
56. Emsley, P., Lohkamp, B., Scott, W. G. & Cowtan, K. Features and development of Coot. *Acta crystallographica. Section D, Biological crystallography* **66**, 486-501 (2010). https://doi.org:10.1107/s0907444910007493
57. Liebschner, D. *et al.* Macromolecular structure determination using X-rays, neutrons and electrons: recent developments in Phenix. *Acta crystallographica. Section D, Structural biology* **75**, 861-877 (2019). https://doi.org:10.1107/s2059798319011471
58. Pettersen, E. F. *et al.* UCSF ChimeraX: Structure visualization for researchers, educators, and developers. *Protein science : a publication of the Protein Society* **30**, 70-82 (2021). https://doi.org:10.1002/pro.3943
59. Wu, T. T. & Kabat, E. A. AN ANALYSIS OF THE SEQUENCES OF THE VARIABLE REGIONS OF BENCE JONES PROTEINS AND MYELOMA LIGHT CHAINS AND THEIR IMPLICATIONS FOR ANTIBODY COMPLEMENTARITY. *Journal of Experimental Medicine* **132**, 211-250 (1970). https://doi.org:10.1084/jem.132.2.211
60. Krissinel, E. & Henrick, K. Inference of macromolecular assemblies from crystalline state. *Journal of molecular biology* **372**, 774-797 (2007). https://doi.org:10.1016/j.jmb.2007.05.022

Table 1

Table 1 is available in the Supplementary Files section.

Figures

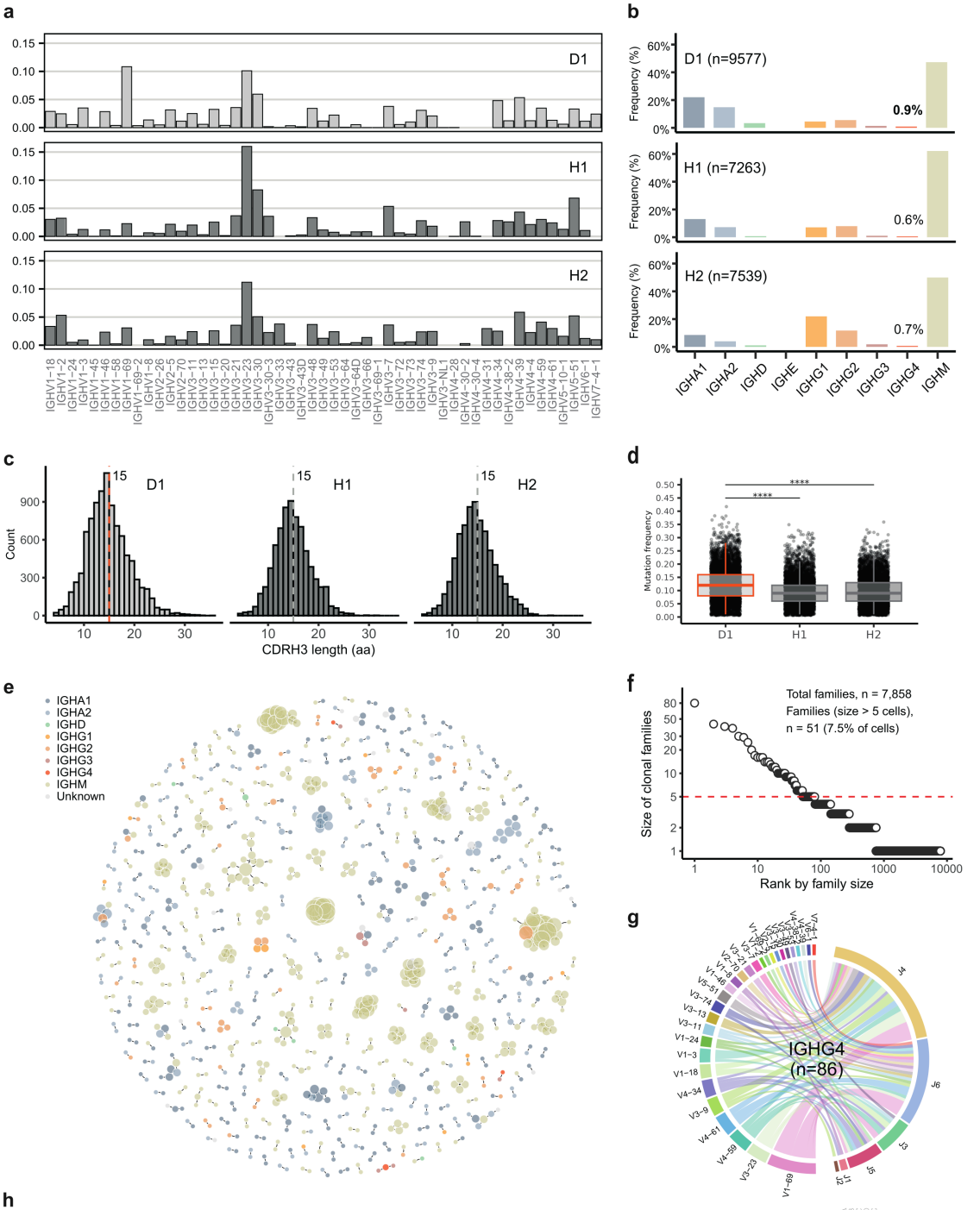

Figure 1

BCR repertoire profiling and clonal architecture of memory B cells in anti-IgLON5 disease. (a) Bar chart showing the frequency of VH gene usage among paired BCRs in memory B cell populations from anti-IgLON5 patient D1 and two healthy donors (H1 and H2). **(b)** Isotype frequency distribution in donors D1, H1, and H2. The total number of clonotypes per donor is indicated in parentheses. The frequency of IgG4 is annotated on the corresponding bar.**(c)** Histogram of CDRH3 length distribution for donors D1, H1 and

H2. Dashed lines indicate median values. **(d)**Boxplot showing somatic mutation frequency (amino acid substitutions relative to V gene germline) across the three donors. Boxes represent the interquartile range (IQR; 25th–75th percentile), with the central line indicating the median. Whiskers extend to 1.5× the IQR, and individual points beyond this range are plotted as outliers. Significant differences were assessed by Welch's ANOVA ($F(2, 14141) = 404$, $p < 0.0001$), with post hoc Games–Howell testing revealing significant differences between D1 and H1 ($p < 0.0001$) and D1 and H2 ($p < 0.0001$), but not between H1 and H2 ($p = 0.087$). **(e)** Clonal network of CDRH3 sequences, coloured by isotype. Clonal families were defined using the Change-O Immcantation toolkit incorporating both heavy and light chains of paired BCRs. Clonal family identifiers were subsequently used as V gene input for edit-distance-based clustering with clonalCluster() (scRepertoire). Node size is proportional to the square root of the number of identical sequences. **(f)**Waterfall plot showing the size distribution of all clonal families. A dashed red line delineates clonal families containing more than five cells from those containing five or fewer cells. **(g)** Chord diagram representing heavy chain V–J gene combinations among IgG4 clonotypes. **(h)**Sequence alignment of the IgLON5-specific monoclonal antibody mAb2513 with its inferred unmutated common ancestor (UCA). Top: heavy chain alignment, VH4-39 and JH4 (D gene region masked and represented as "X"). Bottom: light chain alignment, VK3-20 and JK3. Dots indicate identity with the UCA sequence. Residue positions are numbered according to the Kabat scheme. Red boxes highlight the three Kabat-defined complementarity-determining regions (CDRs).

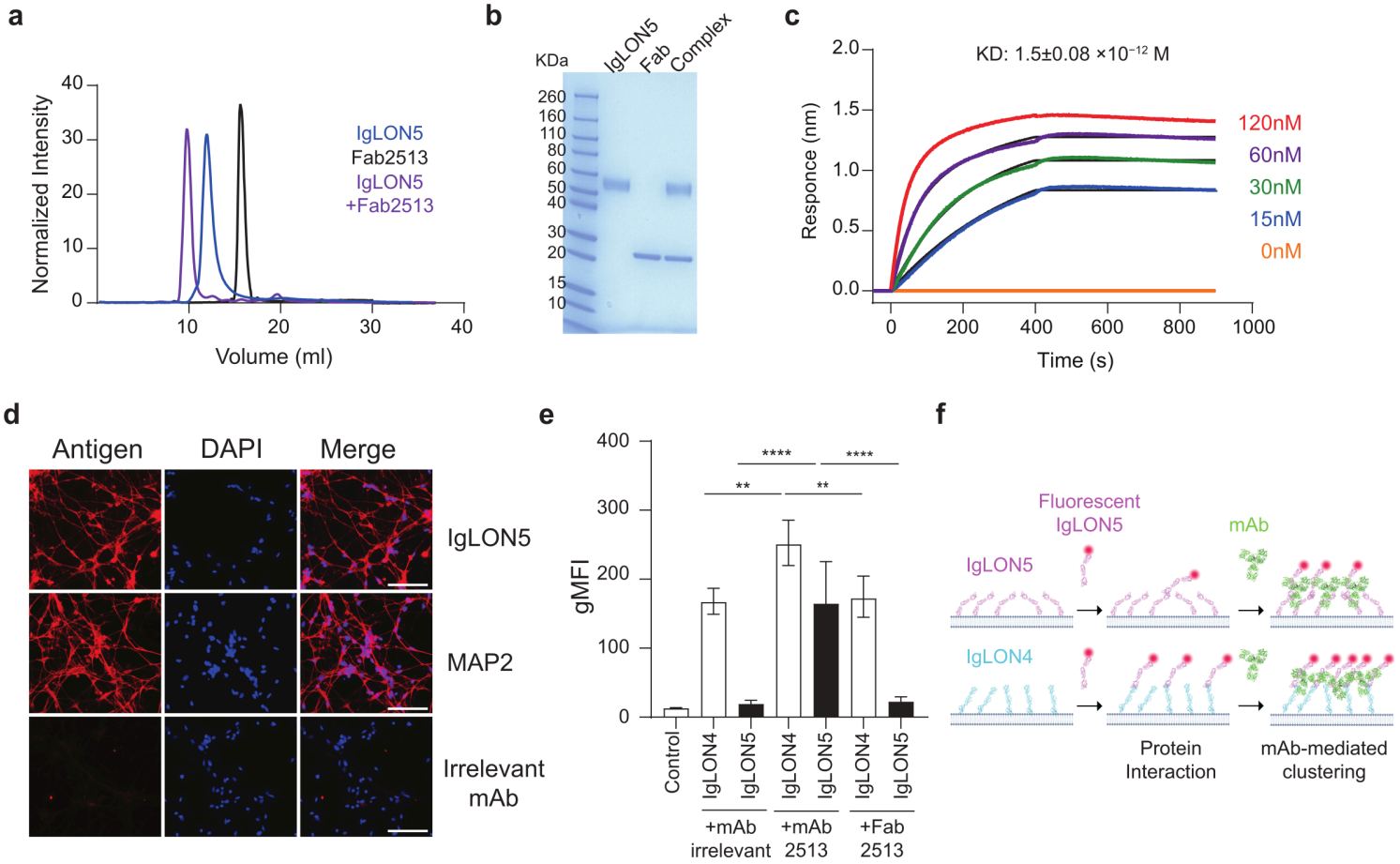

Figure 2

High-affinity interaction of mAb2513 with IgLON5 induces receptor clustering. (a) Size-exclusion chromatography profiles of IgLON5 (blue), Fab2513 (black), and the Fab–IgLON5 complex (violet)**. (b)** SDS–PAGE analysis under reducing conditions of the corresponding peaks. IgLON5 migrates at 55 kDa due to glycosylation, while the reduced Fab fragment migrates at 25 kDa. **(c)** Fab–IgLON5 interaction assessed by biolayer interferometry (BLI). The Fab was immobilized on FAB2G biosensor and exposed to IgLON5 at increasing concentrations (15–120 nM). Binding responses (nm shift) were recorded. The sensorgram shown is representative of at least two independent experiments (n ≥ 2). **(d)** Immunostaining of human stem cell–derived neurons. IgG binding to MAP2-positive or IgLON5-expressing neurons is shown in red, and nuclei (DAPI) in blue. Scale bars, 50 µm.
(e) Geometric mean fluorescence intensity of IgLON4- or IgLON5-transfected SH-SY5Y cells incubated with fluorescent soluble IgLON5 in the presence of an irrelevant antibody, mAb2513, or Fab2513. Control are mock transfected cells incubated with fluorescent soluble IgLON5. Data are presented as geometric mean ± SD from four independent experiments (n = 4). ** $p < 0.01$, **** $p < 0.001$ (one-way ANOVA with Tukey's multiple comparisons test). **(f)** Schematic representation of the potential receptor clustering induced by mAb2513-induced.

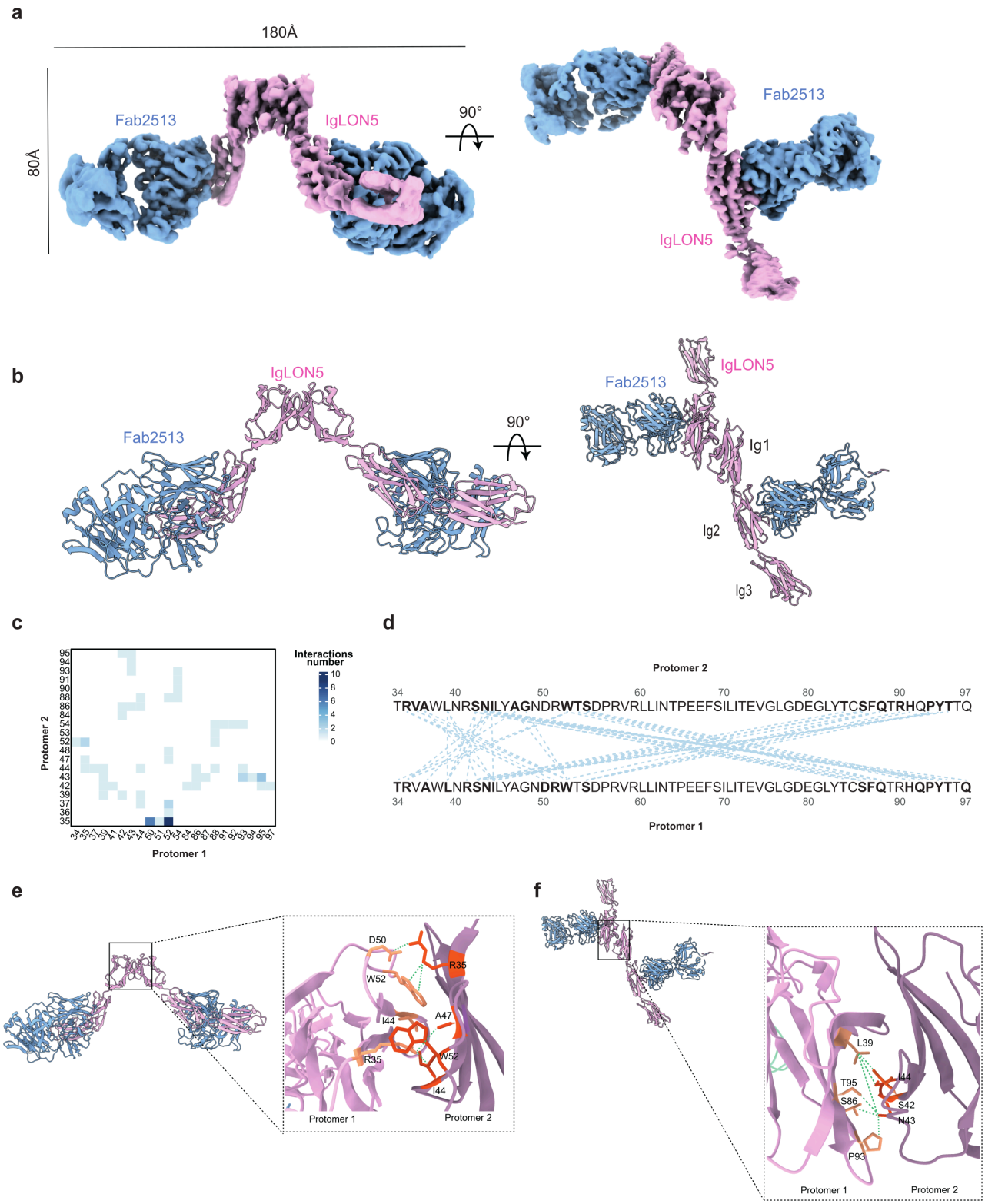

Figure 3

Structural characterization of the IgLON5 dimer bound by Fab2513. (**a**) Side and top views of the cryo-EM density map of two Fab2513 molecules in complex with the IgLON5 dimer, with IgLON5 shown in pink and Fab2513 shown in blue. The overall dimensions of the complex are indicated. (**b**) Atomic model of the complex shown in cartoon representation, with the three Ig domains labelled. (**c**) Heatmap showing the interactions between the two Ig1 domains of the IgLON5 dimer. The number of interactions

is color-coded using a blue gradient. (**d**) 2D representation and sequence of the Ig1 domain for the protomer 1 and 2. Dashed lines indicate hydrogen bonds and salt-bridge interactions. The amino acids involved in the interaction are in bold. (**e**) Close-up view of the interactions involving arginine 35 (R35) and tryptophan 52 (W52). Protomer 1 is shown in pink, with highlighted residues in light orange, and protomer 2 is shown in violet, with highlighted residues in dark orange. (**f**) Close-up view of the interactions between the two protomers centered on leucine 39 (L39), isoleucine 44 (I44), and asparagine 43 (N43).

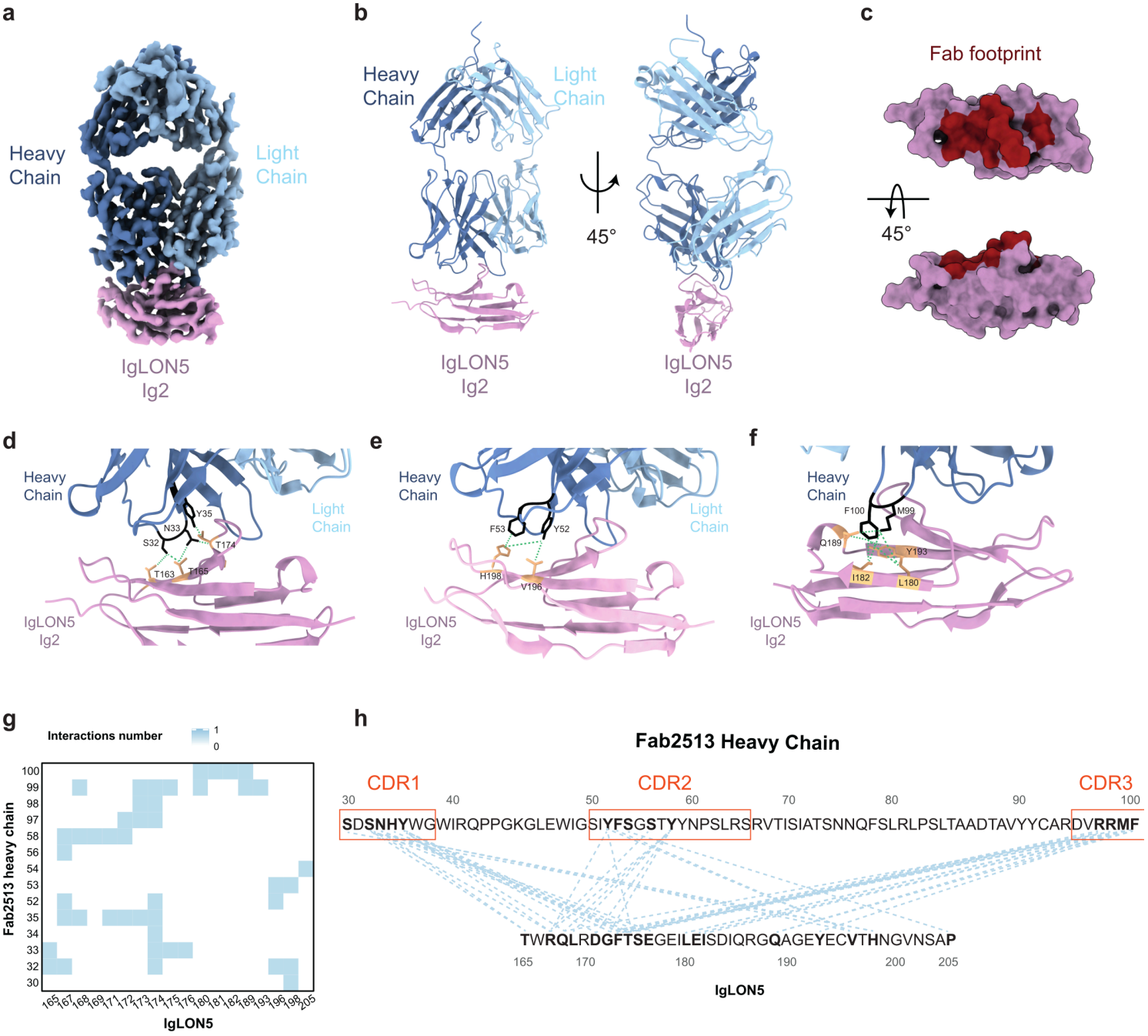

Figure 4

Detailed interaction of Fab2513 with the IgLON5 Ig2 domain. (a) Front view of the locally refined cryo-EM density map of Fab2513 bound to the Ig2 domain of IgLON5. The heavy chain is shown in dark blue,

the light chain in light blue, and Ig2 in pink. **(b)** Atomic model of the Fab–Ig2 complex in cartoon representation, highlighting the pincer-like interaction. **(c)** Surface representation of the Ig2 domain showing the Fab2513 footprint, with contact residues highlighted in dark red. **(d)** Close-up view of interactions involving CDRH1-S32, N33 and Y35 (blue and black) with IgLON5 (orange and pink). **(e)** Close-up view of interactions involving CDRH2-Y52 and F53 (blue and black) on IgLON5 (orange and pink). **(f)** Close-up view of interactions involving CDRH3-M99 and F100 (blue and black) with IgLON5 (orange and pink). **(g)** Heatmap showing interactions between the heavy chain of Fab2513 and residues of the Ig2 domain involved in binding. Residues are numbered according to Kabat. **(h)** Two-dimensional representation of the heavy chain sequence of Fab2513 and part of the Ig2 domain of IgLON5. Dashed lines indicate hydrogen bonds and salt bridge interactions. The amino acids involved in the interaction are in bold.

Supplementary Files

This is a list of supplementary files associated with this preprint. Click to download.

- Table1.docx
- SupplementaryMaterialsRoux.docx
- PDBvalidationreport.pdf